JOURNAL OF THE MECHANICAL BEHAVIOR OF BIOMEDICAL MATERIALS 36 (2014) 120–134

Available online at www.sciencedirect.com

ScienceDirect

www.elsevier.com/locate/jmbbm


Research Paper

# Prediction of Young's modulus of trabeculae in microscale using macro-scale's relationships between bone density and mechanical properties

Łukasz Cyganik[a], Marcin Binkowski[a,*], Grzegorz Kokot[b], Tomasz Rusin[c], Paulina Popik[a], Filip Bolechała[d], Roman Nowak[e], Zygmunt Wróbel[a], Antoni John[b]

[a]X-ray Microtomography Lab, Department of Biomedical Computer Systems, Institute of Computer Science, Faculty of Computer and Materials Science, University of Silesia, 75 Pulku Piechoty 1, budynek H, segment C, pok. P7, 41-500 Chorzów, Poland
[b]Institute of Computational Mechanics and Engineering, Silesian University of Technology, ul. Konarskiego 18A, 44-100 Gliwice, Poland
[c]Elhys Sp. z o.o., MTS Systems Corporation Representative in Poland, ul. Naukowa 45, 02-463 Warszawa, Poland
[d]Medical College, Jagiellonian University, ul. Grzegórzecka 16, 31-531 Kraków, Poland
[e]Medical University of Silesia, School of Medicine with the Division of Dentistry, Chair and Department of Orthopaedics, WSS no. 5, ul. Medyków 1, 41-200 Sosnowiec, Poland

ARTICLE INFO

*Article history:*
Received 9 January 2014
Received in revised form
17 April 2014
Accepted 20 April 2014
Available online 29 April 2014

*Keywords:*
Trabecular bone
Young's modulus
Micro-computed tomography
Bone mineral density
Digital Image Correlation
Microscale properties

ABSTRACT

According to the literature, there are many mathematical relationships between density of the trabecular bone and mechanical properties obtained in macro-scale testing. In micro-scale, the measurements provide only the ranges of Young's modulus of trabeculae, but there are no experimentally tested relationships allowing the calculation of the distribution of Young's modulus of trabeculae within these experimental ranges. This study examined the applicability of relationships between bone density and mechanical properties obtained in macro-scale testing for the calculation of Young's modulus distribution in micro-scale. Twelve cubic specimens from eleven femoral heads were cut out and micro-computed tomography (micro-CT) scanned. A mechanical compression test and Digital Image Correlation (DIC) measurements were performed to obtain the experimental displacement and strain full-field evaluation for each specimen. Five relationships between bone density and Young's modulus were selected for the test; those were given by Carter and Hayes (1977), Ciarelli et al. (2000), Kaneko et al. (2004), Keller (1994) for the human femur, and Li and Aspden, 1997. Using these relationships, five separate finite element (FE) models were prepared, with different distribution of Young's modulus of trabeculae for each specimen. In total, 60 FE analyses were carried out. The obtained displacement and strain full-field measurements from numerical calculations and

Abbreviations: micro-CT, micro-computed tomography; DIC, Digital Image Correlation; FEM, finite element method; FEA, finite element analysis; BMD, bone mineral density; MTD, main trabecular direction; GD, grey density; HAD, hydroxyapatite density

*Corresponding author. Tel.: +48 887760522.
*E-mail address:* marcin.binkowski@us.edu.pl (M. Binkowski).

http://dx.doi.org/10.1016/j.jmbbm.2014.04.011

experiment were compared. The results indicate that the highest accuracy of the numerical calculation was obtained for the Ciarelli et al. (2000) relationship, where the relative error was 17.87% for displacements and 50.94 % for strains. Therefore, the application of the Ciarelli et al. (2000) relationship in the microscale linear FE analysis is possible, but mainly to determine bone displacement.



## 1. Introduction

In clinical practice, the gold standard of non-invasive assessment of bone structure is the evaluation of bone mineral density (BMD) as recommended by the World Health Organization (WHO) (Kanis et al., 2000; WHO, 1994). As a result only partial estimation of patients' bone condition is obtained, which directly affects the probability of future osteoporotic lesions. Application of densitometry without additional testing in the mechanical context does not allow a full description and evaluation of the trabecular bone micro-architecture. A number of histomorphometric parameters describing bone tissue, determined on the basis of tomographic imaging, should be the set of input data for the three-dimensional model of cancellous bone structure followed by mechanical testing analysis using FEA.

The basic technique for providing high-resolution data translating into high accuracy of calculations performed on their basis is micro-computed tomography. Micro-computed tomography (micro-CT) and computed tomography (CT) are methods commonly used in clinical studies (Binkowski et al., 2010; Muller et al., 1998; Rüegsegger et al., 1996; Shefelbine et al., 2005; Ulrich et al., 1998), laboratory studies (Lin et al., 2003; McDonald et al., 2003; Mercer et al., 2003; van Garderen et al., 2012) as well as in industry (Badde and Illerhaus, 2008). Micro-CT delivers high resolution of the cross-sectional images, which can also be processed to three-dimensional views based on surface or volume rendering. CT and micro-CT scans combined with the finite element method (FEM) are powerful tools for prediction of the mechanical properties of the bone (Depalle et al., 2013; Hambli, 2013; Kokot et al., 2012). Especially interesting is the use of multiscale FEM simulations, which allow one to achieve a significantly better accuracy than the one-scale simulations (Makowski et al., 2013). However, the multiscale simulations require a preparation of FE models individually for each of the scale, which is associated with the appropriate selection of Young's modulus and Poisson's ratio in the numerical model. The selection of Young's modulus has a great influence on the accuracy of finite element analysis (FEA) and requires special relationships between Young's modulus and tissue density, which allow one to obtain Young's modulus from the micro-CT scans. According to the literature, there are many mathematical relationships between bone density and mechanical properties established on the basis of research in a macro-scale (Carter and Hayes, 1977; Ciarelli et al., 2000; Helgason et al., 2008; Kaneko et al., 2004; Keller, 1994; Keyak et al., 1994; Li and Aspden, 1997). Macro-scale refers to mechanical compression tests on cylindrical or cubic specimens (Carter and Hayes, 1977; Ciarelli et al., 2000; Kaneko et al., 2004; Keller, 1994; Li and Aspden, 1997). Most of these relationships work well in predicting the mechanical behavior of bone in the range of applicability defined by the authors. Micro-scale refers to Young's modulus of trabeculae measured by nanoindentation, 3-point microbending test, compression test of microscopic cubic specimens or uniaxial testing of single trabeculae (Choi et al., 1990; Hong et al., 2007; Jiroušek et al., 2011; Rho et al., 1997; Turner et al., 1999; Zysset et al., 1999). In micro-scale, there is no appropriate relationship that would allow for the accurate prediction of the mechanical behavior of trabeculae. There is only one theoretical relationship given by Wagner et al. (2011), which is included in their theory of determining the voxel-specific tissue density by means of micro-CT data.

However, in this article we focused on finding a mathematical relationship that will allow for the accurate prediction of Young's modulus of trabeculae in the micro-scale. One of the possibilities is treating the relationships estimated in the macro-scale only as a mathematical function without taking into account the ranges of applicability defined by the authors. Then the applicability of these mathematical functions in micro-scale should be verified experimentally. For this purpose, an experiment should be performed (e.g., bone compression test), and then a numerical simulation of the same experiment performed, where Young's modulus values will be calculated and assigned to the finite element (FE) models using mathematical functions that are verified. Finite elements should build micro-scale components such as trabeculae. We expect that a good compatibility between experimental and numerical results will be achieved, if Young's modulus distributions calculated from mathematical functions are similar to Young's modulus ranges of trabeculae measured in micro-scale. Such experimental measurements of Young's modulus of trabeculae depend on the measurement technique and measurement conditions (wet/dry) used in research. Nanoindentation measurements in dry conditions were used for example by Rho et al. (1997), Turner et al. (1999) and Jiroušek et al. (2011), who also compared nanoindentation results with the results of uniaxial testing of single trabeculae. Young's modulus ranges given by these authors were $13.4\pm2.0$ GPa, $18.14\pm1.7$ GPa and $16.34\pm1.76$ GPa (nanoindentation)/$9.21\pm1.26$ GPa (uniaxial testing), respectively. The measurements in wet conditions were performed by Choi et al. (1990) using the 3-point microbending test, Hong et al. (2007) using the compression test of microscopic cubic specimens and Zysset et al. (1999) using nanoindentation. Young's modulus ranges were 3.27–10.58 GPa, $3.47\pm0.41$ GPa and $11.4\pm\pm5.6$ GPa, respectively. The above-mentioned experimental ranges overlap partially, but in general the differences between them are significant. Thus, the question is which experimental range should be used in numerical modeling and

how to calculate the distribution of Young's modulus of trabeculae within this range.

The aim of the present study was to examine the applicability of the relationships between Young's modulus and bone density, which were obtained in macro-scale testing for the calculation of Young's modulus distribution in micro-scale. In addition, the present study is an attempt to find out which of the relationships is the optimal one for predicting bone mechanical behavior.

## 2. Material and methods

### 2.1. *Specimen preparation*

Nine femoral heads from patients undergoing total hip replacement surgery (Provincial Specialist Hospital No. 5 in Sosnowiec, Poland) and two proximal ends of the human femur from cadavers (Department of Forensic Medicine, Jagiellonian University Medical College in Cracow, Poland) were obtained. The donors were aged 45–77. The hip specimens from the hospital were collected with permission from the Bioethics Committee from the Medical Silesian University in Katowice, Poland. Hip degenerative disease was diagnosed in eight of them, dysplasia and necrosis in one, in another there was a femoral neck fracture; for the last two no diagnosis information was available [see Table 1]. Cubic specimens (total number=12) for mechanical testing were cut out from the femoral heads, using a precision saw machine with a diamond-coated cut-off wheel (STRUERS Secotom – 15, Willich, Germany, 2200 rpm, $f$=0.1 mm/s). The cutting planes of the femoral heads were located at the thinnest point of the femoral neck and were perpendicular to the femoral neck axis (Fig. 1a). The main trabecular direction (MTD) was identified and marked on the femoral head using the CT scans. The trabecular bone layers were cut out of the femoral heads according to MTD (Fig. 1b). The target thickness of the layers was 10 mm. MTD was marked on the layers again, and the cubic specimens were cut out of these layers. The orientation of the specimens in the femoral heads was marked. The specimens' planes parallel to the anterior–posterior axis were marked with a single dot, and the planes perpendicular to MTD were marked with two dots. The specimens were divided into two categories: “core” and “side”. The specimens located in the center of the layer, which had a vertical direction of trabeculae, were classified into the “core” category (number of specimens=7) (Table 1, Fig. 1c). The other specimens located in one of the sides of the layer, which had a diagonal direction of trabeculae, were classified into the “side” category (number of specimens=5). The specimens were fixed in 70% ethanol and stored in 4 °C between research to reduce the risk of infection. The procedure of specimen's cutting, micro-CT scanning and mechanical testing lasted about 2 days. The time of specimen's fixation in ethanol was several hours.

Distribution of the mechanical parameters in the femoral head region is widely known (Augat et al., 1998; Łukowski et al., 2000). Therefore, for the purpose of this study samples from different regions were distinguished using the “side” and “core” categorization.

**Table 1 – Specimen data.**

| No. | Specimen no. | Sex | Age | Side | Diagnosis | Specimen position in femur head | Specimen dimensions | | |
|---|---|---|---|---|---|---|---|---|---|
| | | | | | | | Length | Width | Height |
| 1 | 8AII | M | 45 | Left | Left hip degenerative disease | Side | 10.5 | 11.3 | 10.7 |
| 2 | 12AI | M | 64 | Right | Both hips degenerative disease | Side | 10.4 | 10.4 | 10.7 |
| 3 | 12BII | M | 64 | Right | Both hips degenerative disease | Core | 10.4 | 10.4 | 10.7 |
| 4 | 13BII | F | 62 | Right | Right hip degenerative disease | Core | 10.4 | 10.4 | 10.4 |
| 5 | 14AII | F | 74 | Left | Left hip degenerative disease | Core | 10.4 | 10.4 | 10.7 |
| 6 | 15AII | M | 54 | Right | Right hip degenerative disease | Core | 10.4 | 10.4 | 10.4 |
| 7 | 16BII | F | 70 | Left | Left hip degenerative disease | Core | 10.4 | 10.5 | 10.4 |
| 8 | 17AII | F | 69 | Right | Femoral neck fracture | Side | 10.4 | 10.4 | 10.4 |
| 9 | 18CI | F | 59 | Left | Dysplasia, necrosis | Core | 10.4 | 10.4 | 10.9 |
| 10 | 20BII | M | 46 | Left | Left hip degenerative disease | Core | 10.3 | 10.4 | 10.4 |
| 11 | 23AI | M | 75 | Left | No data | Side | 10.3 | 10.4 | 10.7 |
| 12 | 24AII | M | 77 | Right | No data | Side | 10.3 | 10.5 | 10.5 |

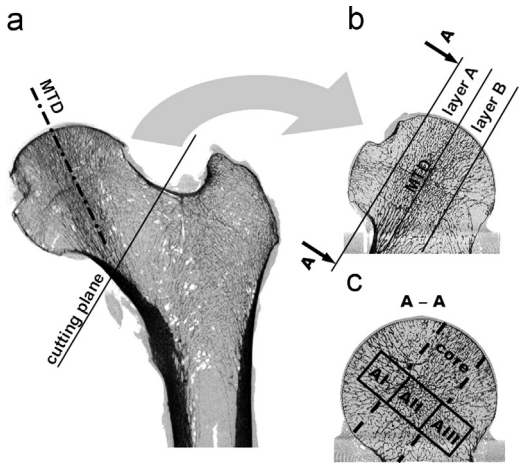


**Fig. 1 – Micro-CT cross-sections for femur no. 12. (a) Proximal end of the femur, showing the main trabecular direction (MTD) and the position of cutting plane. (b) Position of layers in the femoral head and the position of A–A cross-section. (c) A–A cross-section showing the surface of layer A with marked position of specimens: 12AI, 12AII and 12AIII. The area between the dashed lines is classified into the "core" category.**

### 2.2. *Quantitative micro-computed tomography scanning*

All the femoral heads were scanned with a micro-CT scanner (v|tome|x s, GE Sensing & Inspection Technologies, Phoenix|x-ray, Wunstorf, Germany). The device is a laboratory scanner (also called an industrial scanner) consisting of two open X-ray tubes: direct tube (240 kV) and transmission nano-tube (180 kV). In this study the direct tube was applied. It is equipped with both tungsten cathode (filament) and anode (target), and the polychromatic X-ray cone-beam is used there. The results of X-ray beam attenuation propagated through the sample located on the rotary table in the scanner chamber is recorded by the 16″ Flat Panel Detector (2024 × 2024 pixels, pixel size = 200 μm$^2$). The manufacturer's software (Datos 2.0) was applied to obtain projection and image reconstruction.

The femoral heads were scanned to obtain the view of the total specimen in order to identify the main trabecular direction (MTD). Having the proper orientation of MTD, the cubic samples dissected from the specimen were tested using higher scanning resolution. The scanning parameters are presented in Table 2.

A hydroxyapatite phantom was used while scanning all the cubic specimens. The density phantom is a custom-made product designed by authors a few years back and ordered to manufacture by QRM (QRM GmbH, Moehrendorf, Germany). The phantom is delivered with individual protocol described amount of HA in each cylinder. The quality of phantom was a subject of previous studies (Binkowski et al., 2012, 2010). The phantom consists of 5 cylinders of varied HA concentrations (100, 200, 400, 800, and 1000 mg HA/cm$^3$). The cylinders are held parallel to each other in the resin cube. The mean gray density values (GD) for every cylinder were calculated against the known mineral density at each cross-section of the dataset, and individual linear calibration curves for each sample were estimated as follows: based on the images of individual samples obtained from micro-CT in the ImageJ 1.44p (Wayne Rasband, National Institutes of Health, USA), GD were calculated in correlation with the hydroxyapatite density (HAD, g/cm$^3$). Then the $\alpha$ and $\beta$ coefficients of linear calibration curves were estimated for each sample (Table 3). The calibration curves were applied to calculate the Quantitative Bone Mineral Density ($\rho_{qBMD}$) parameter (Eq. 1), which defines the mineral density of bone in each cubic sample as an equivalent of HA:

$$\rho_{qBMD} = \alpha GD + \beta \, [g/cm^3] \quad (1)$$

**Table 2 – Scan parameters of femoral heads and the specimens.**

| Scan parameters | | |
|---|---|---|
| Parameter | Femur heads | Specimens |
| Magnification | 5.985 | 19.518 |
| Voxel size [μm] | 33.416 | 10.246 |
| Binning | – | – |
| FOD [mm] | – | 48.08 |
| FDD [mm] | – | 938.54 |
| Scan time [min] | 34 | 26 |
| Number of images | 1000 | 1000 |
| Image width | 2024 | 2024 |
| Image height | 2024 | 2024 |
| Fast scan | No | No |
| Type | Microfocus | Microfocus |
| Timing [ms] | 500 | 500 |
| Average | 3 | 2 |
| Skip | 1 | 1 |
| Voltage [kV] | 140 | 70 |
| Current [μA] | 200 | 140 |
| Mode | 0 | 0 |
| Filter | Cu 0.5 | Cu 0.1 |
| Phantom | 2.2 | 2.2 |

**Table 3 – Coefficients of Eq. (1).**

| Specimen no. | Coefficients | |
|---|---|---|
| | $\alpha$ | $\beta$ |
| 8AII | 0.07 | −2.589 |
| 12AI | 0.022 | −2.346 |
| 12BII | 0.019 | −1.92 |
| 13BII | 0.02 | −2.008 |
| 14AII | 0.019 | −1.686 |
| 15AII | 0.02 | −2.075 |
| 16BII | 0.021 | −2.343 |
| 17AII | 0.02 | −1.849 |
| 18CI | 0.018 | −1.772 |
| 20BII | 0.04 | −1.567 |
| 23AI | 0.019 | −1.515 |
| 24AII | 0.023 | −2.485 |

### 2.3. *Mechanical testing and Digital Image Correlation (DIC)*

The specimens were mechanically tested in a uniaxial compression test using a platen technique on an MTS machine (MTS Insight 2, Eden Prairie, MN, USA). Digital Image Correlation system (model Q-400, Dantec Dynamics GmbH,

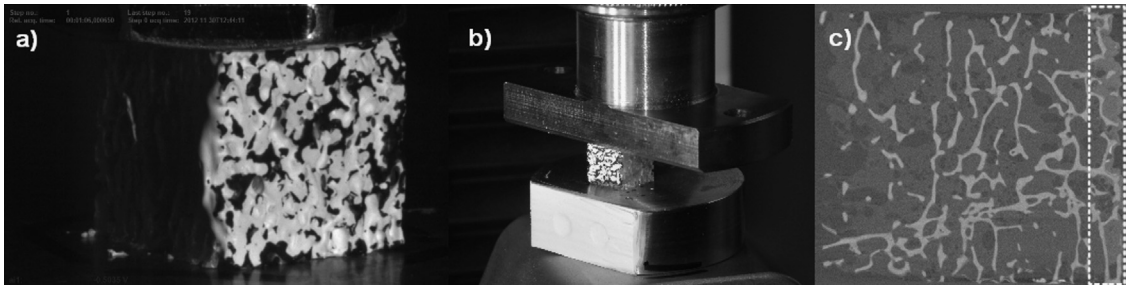


**Fig. 2 – Specimen no. 13BII. (a) Front surface prepared for DIC measurement. (b) Specimen during compression test and (c) the micro-CT cross section of the specimen with indicated (white dashed frame) region of acrylic paint penetration.**

Ulm, Germany) was used to measure displacement and strain fields in two axes ($x$, $y$) during the compression test.

Digital Image Correlation technique uses a special image correlation algorithm, based on a pseudo-affine coordinate transformation from one camera image to another for full-field displacement and strain evaluation. This algorithm compares the so-called facets of digitized images obtained by observing the specimen surface with two digital cameras while loading. The position of each point of an object in three dimensions is calculated based on knowledge of the imaging parameters for each camera and their mutual orientation. As the series of measurements is taken, while the specimen surface is moved due to loading, the displacements and strains on the object surface can be assessed. What is specific for this method is that the specimen surface must have a randomly generated speckle pattern on it, which is used to track the facets. On this ground the correlation algorithm transforms the corresponding facet positions in both cameras into 3D coordinates for each step, resulting in tracking of each facet surface in 3D space. It is the basis for the displacement and strain evaluation by the image correlation algorithm (Becker et al., 2006).

To perform measurements, the cubic specimens were painted with non-toxic white acrylic paint (background paint) by means of a paintbrush. Black acrylic paint was used to create a stochastic speckle pattern (Fig. 2a), which was sprayed from a distance of 20 mm. Only one side surface of each specimen was painted. The mean speckle size was 0.3 mm and there were in average about 200 speckles per specimen surface (10 mm × 10 mm). Fig. 2c indicates in a white dashed frame a region of penetration of acrylic paint into the trabecular bone. The mean depth of the penetration equaled to less than 1 mm. The orientation of all the specimens in the compression test was the same, and the direction of compression corresponded to the MTD. The specimen's surface used for the DIC measurement was parallel to the anterior–posterior (AP) axis. The compression tests were performed at the displacement rate of 0.5 mm/min at room temperature (≈25 °C). The load range was from 0 to 2000 N (or till the specimen's failure). The pre-load of specimens was 1 N. The DIC system was set up to take pictures every 100 N of the force increment.

### 2.4. *Selection of relationships between bone density and Young's modulus*

Five relationships between bone density and Young's modulus were selected for the tests; those were given by Carter and Hayes (1977), Ciarelli et al. (2000), Kaneko et al. (2004), Keller (1994) and Li and Aspden (1997) (Fig. 3, Table 4). The decision about the selection of the relationships was made based on the significant differences between the coefficients of the functions describing these relationships. Young's modulus range of the relationships and the fact that most of them were estimated in research on the human femur (except Carter and Hayes, 1977, which was estimated in pooled site research) were also taken into account. In addition, cubic specimens were used in three of them: the ones given by Keller (1994), Ciarelli et al. (2000) and Kaneko et al. (2004). In the other two cylindrical specimens were used. In majority of the selected relationships Young's modulus range at least partially corresponded to the experimental Young's modulus ranges given by Choi et al. (1990), Hong et al. (2007) or Zysset et al. (1999).

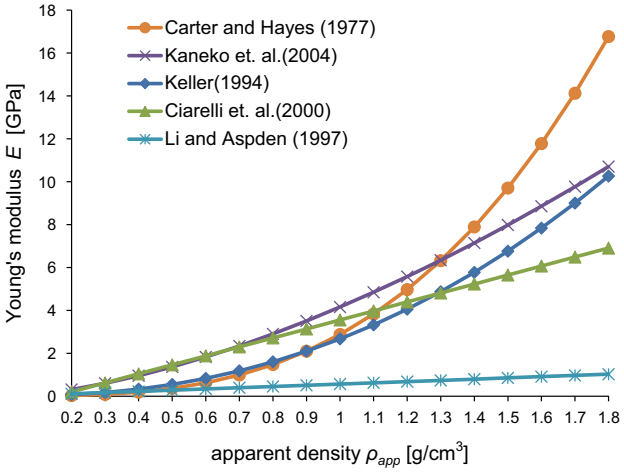


**Fig. 3 – Relationships between density and Young's modulus selected for the tests (Helgason et al., 2008).**

Having selected the relationships, the required variables were calculated as follows. The first step was to determine the distribution of quantitative bone mineral density $\rho_{qBMD}$ in each specimen using the GD values from the micro-CT scans and the previously calculated $\alpha$ and $\beta$ coefficients (Eq. 1). Then, the quantitative bone mineral density $\rho_{qBMD}$ was an input data to calculate the distribution of ash density $\rho_{ASH}$. In order to calculate the distribution of ash density $\rho_{ASH}$ Eq. (2) provided by Kaneko et al. (2004) for the no cancer (NC) group of specimens was used (Helgason et al., 2008; Kaneko et al., 2004). The ash density $\rho_{ASH}$ was used for the calculation of

**Table 4 – Relationships between density and Young's modulus selected for the tests (Helgason et al., 2008).**

| Study | Site | Specimen's shape | Densitometric measure | $\rho$-Range [g/cm$^3$] | Young's modulus function E [GPa] |
|---|---|---|---|---|---|
| Carter and Hayes (1977) | Pooled | cylindrical | $\rho_{app}$ | 0.07–2.0 | $E = 3.79\dot{\varepsilon}^{0.06}\rho_{app}^{3}$ |
| Keller (1994) | Femur | Cubic | $\rho_{ash}$ | 0.092–1.221 | $E = 10.5\rho_{ash}^{2.29}$ |
| Li and Aspden (1997) | Femoral head | Cylindrical | $\rho_{app}$ | 0.14–1.4 | $E = 0.573\rho_{app} - 0.0094$ |
| Ciarelli et al. (2000) | Proximal femur | Cubic | BV/TV | 0.15–0.40$^{RFG}$ | $E = 7.541(BV/TV) - 0.637$ |
| Kaneko et al. (2004) | Distal femur | Cubic | $\rho_{ash}$ | 0.102–0.331 | $E = 10.88\,\rho_{ash}^{1.61}$ |

Young's modulus (E) in GPa and density in g/cm$^3$. RFG = read from graph.

**Table 5 – Numerical models data.**

| Specimen no. | Type of element | Number of elements | Number of different $E_{ij}^{(sn)}$ values | Load [N] |
|---|---|---|---|---|
| 8AII | Tet10 | 1,114,130 | 11 | 1200 |
| 12AI | Tet10 | 769,950 | 11 | 600 |
| 12BII | Tet10 | 853,516 | 10 | 1200 |
| 13BII | Hex8 | 1,119,803 | 8 | 1020 |
| 14AII | Hex8 | 1,126,503 | 8 | 1000 |
| 15AII | Tet10 | 1,069,141 | 10 | 1000 |
| 16BII | Hex8 | 1,242,083 | 11 | 1000 |
| 17AII | Hex8 | 751,447 | 11 | 700 |
| 18CI | Tet10 | 935,911 | 10 | 900 |
| 20BII | Tet10 | 1,087,268 | 12 | 1000 |
| 23AI | Hex8 | 870,917 | 9 | 627 |
| 24AII | Tet10 | 802,708 | 11 | 1200 |

Young's modulus of two relationships: those given by Keller (1994) and Kaneko et al. (2004). In the other three relationships, which are the functions of apparent density $\rho_{app}$ (Carter and Hayes, 1977; Li and Aspden, 1997) or bone volume fraction BV/TV (Ciarelli et al., 2000), Eqs. (3) and (4)[1] were used (Helgason et al., 2008; Keyak et al., 1994).

$$\rho_{ASH} = 79.8 + 0.792\rho_{qBMD}\ (\mathrm{mg/cm^3}) \tag{2}$$

$$\rho_{app} = \frac{\rho_{ASH}}{0.55}\ (\mathrm{g/cm^3}) \tag{3}$$

$$BV/TV = \frac{\rho_{app}}{1.8}\ (\mathrm{g/cm^3}) \tag{4}$$

Young's modulus relationships were considered only as mathematical functions, without taking into account the $\rho$ – ranges of these relationships given by the authors (Table 4). The reason for this methodology is that the range of applicability of the relationships in microscale was the subject of the research. Therefore, although the $\rho_{ASH}$, $\rho_{app}$ or BV/TV values exceeded the $\rho$ – ranges given by the authors, we used them in the numerical model.

### 2.5. *Numerical model*

The trabecular bone structures were segmented from each of the micro-CT scans, and then the 3D bone surface models were created. The 3D bone surface models were optimized using the surface smoothing and wrapping operations. Finite element meshes were created with two different methods: directly converting each bone voxel into an eight-noded hexahedral element (Hex8), or by generating the mesh from the 3D bone surface model using a ten-noded tetrahedral element (Tet10). FE meshes and 3D bone surface models were created using Mimics 15.0 (HEX8) and 3-matic (Tet10) software (Materialise, Leuven, Belgium). The number of elements for each specimen's mesh is presented in Table 5. Young's modulus distributions were calculated using the GD values from the micro-CT scans, formulas (1)–(4) and the five selected Young's modulus relationships. Therefore, five meshes for each specimen's model were created, which differed only with the distribution of Young's modulus values ($E_i^{(sn)}$, $sn$ – specimen's number, $i = 1, 2, \ldots, 5$) according to one of the selected relationships. In total, 60 numerical models were generated. Each of the five meshes for one specimen had the same mesh structure. Young's modulus distributions ($E_i^{(sn)}$) were calculated using the uniform material assignment method implemented in the Mimics 15.0, in which the calculation procedure was performed using the following manufacturer protocol. The GD range for each micro-CT scan was divided into 20 intervals and the center GD value in each interval was chosen as a representative for that material ($GD_{ij}^{(sn)}$, $i = 1, 2, \ldots, 5$, $j = 1, 2, \ldots, 20$). Young's modulus value in each interval was calculated using the representative GD value [$E_{ij}^{(sn)}(GD_{ij}^{(sn)})$, $i = 1, 2, \ldots, 5$, $j = 1, 2, \ldots, 20$]. Therefore, Young's modulus distribution could have had a maximum

[1] Based on the assumption that real density is equal to compact bone density, i.e. 1.8 g/cm$^3$ (Carter and Hayes, 1977; Helgason et al., 2008).

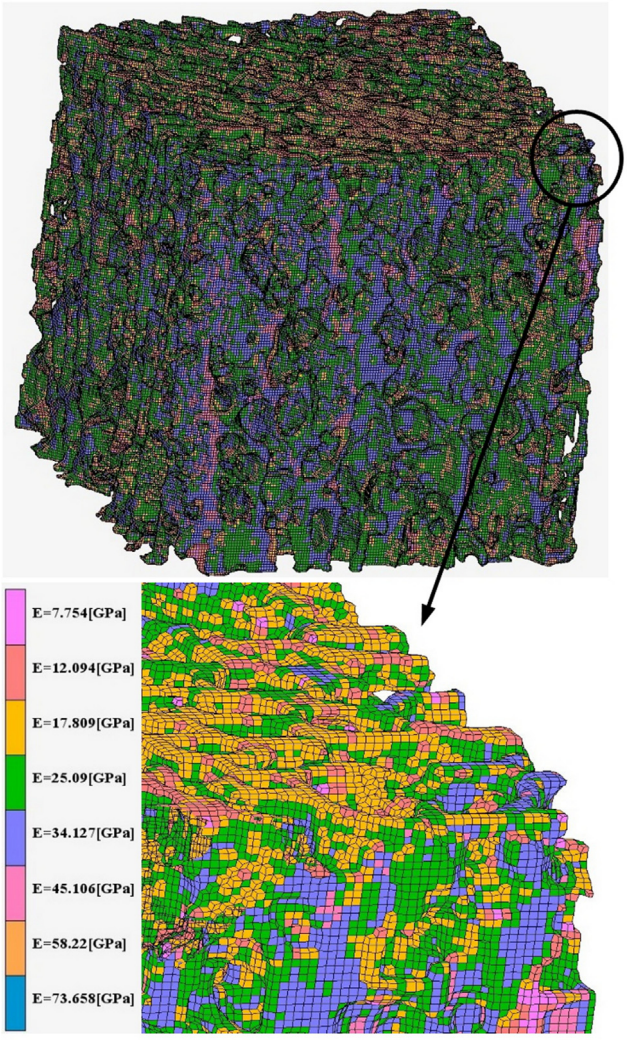


**Fig. 4 – Young's modulus distribution obtained for the relationship given by Carter and Hayes (1977) for specimen no. 13BII.**

number of 20 different Young's modulus values. However, the real number of different Young's modulus values ($E_{ij}^{(sn)}$) was within the range of 8–12 (Fig. 4, Tables 5 and 6). It was due to the used algorithm of dividing the GD range, which is taking the starting GD=0 instead of the minimal GD in the segmented micro-CT images. Poisson's ratio of 0.3 was used.

The FE models had the same orientation during simulation as the specimens during the experiment, and the boundary conditions were also the same for all models and represented the experimental uniaxial compression tests. The FE mesh was virtually placed between two plates. The glue contact was used between the mesh elements and the plate surfaces with a contact tolerance of 0.01 mm. The bottom plate was fixed, but the top plate was free to move with the applied load. The load values for the tested models are presented in Table 5. The numerical analysis was performed only in the elastic range. Therefore, the load was applied in a single step of calculation, but only for the models that had a constant contact area. If there was a relief on the top mesh surface, the initial contact was applied to the highest point of the mesh and changed with

**Table 6 – Example of Young's modulus distributions obtained for specimen no. 13BII.**

13BII – Young's modulus distributions

| j-Index | Number of elements | Ciarelli et al. (2000) | | Keller (1994) | | Kaneko et al. (2004) | | Carter and Hayes (1977) | | Li and Aspden (1997) | |
|---|---|---|---|---|---|---|---|---|---|---|---|
| | | BV/TV | $E_{1j}^{(13BII)}$ [GPa] | $\rho_{ash}$ | $E_{2j}^{(13BII)}$ [GPa] | $\rho_{ash}$ | $E_{3j}^{(13BII)}$ [GPa] | $\rho_{app}$ | $E_{4j}^{(13BII)}$ [GPa] | $\rho_{app}$ | $E_{5j}^{(13BII)}$ [GPa] |
| 1 | 5211 | 0.773 | 5.195 | 0.766 | 5.696 | 0.766 | 7.077 | 1.392 | 7.754 | 1.392 | 0.788 |
| 2 | 39,286 | 0.897 | 6.126 | 0.888 | 7.996 | 0.888 | 8.984 | 1.614 | 12.094 | 1.614 | 0.916 |
| 3 | 160,548 | 1.02 | 7.057 | 1.01 | 10.745 | 1.01 | 11.058 | 1.837 | 17.81 | 1.837 | 1.043 |
| 4 | 406,704 | 1.144 | 7.988 | 1.132 | 13.958 | 1.132 | 13.291 | 2.059 | 25.091 | 2.059 | 1.17 |
| 5 | 462,358 | 1.267 | 8.92 | 1.255 | 17.652 | 1.255 | 15.676 | 2.281 | 34.127 | 2.281 | 1.298 |
| 6 | 44,373 | 1.391 | 9.851 | 1.377 | 21.841 | 1.377 | 18.,208 | 2.503 | 45.107 | 2.503 | 1.425 |
| 7 | 1005 | 1.514 | 10.782 | 1.499 | 26.538 | 1.499 | 20.88 | 2.726 | 58.221 | 2.726 | 1.552 |
| 8 | 318 | 1.638 | 11.713 | 1.621 | 31.757 | 1.621 | 23.689 | 2.948 | 73.658 | 2.948 | 1.68 |

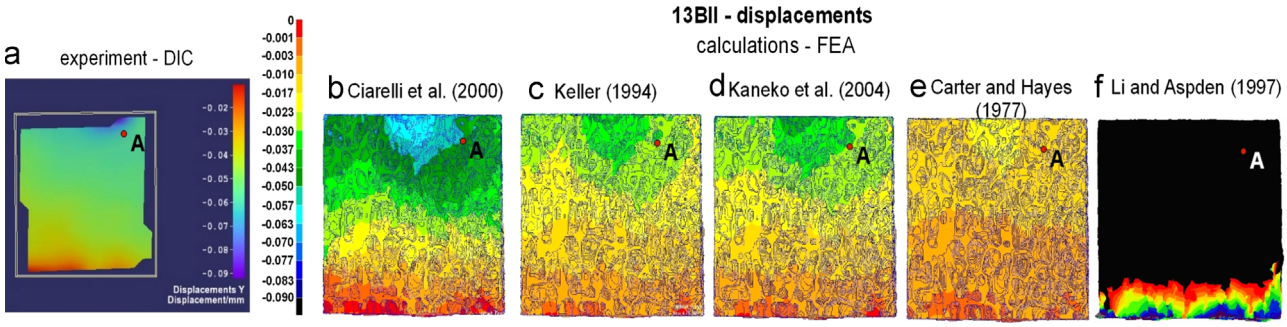


**Fig. 5 – Comparison of displacement distributions obtained from (a) experiment (DIC) and (b–f) numerical analyses (FEA) for specimen no. 13BII.**

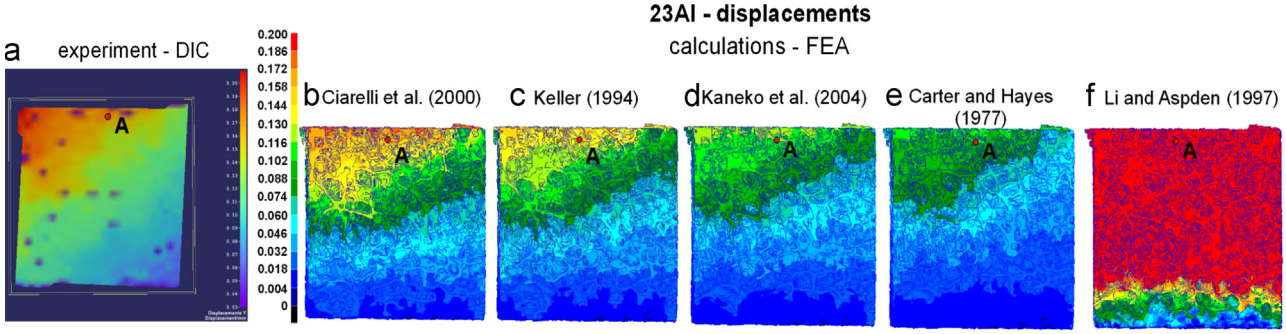


**Fig. 6 – Comparison of displacement distributions obtained from (a) experiment (DIC) and (b–f) numerical analyses (FEA) for specimen no. 23AI.**

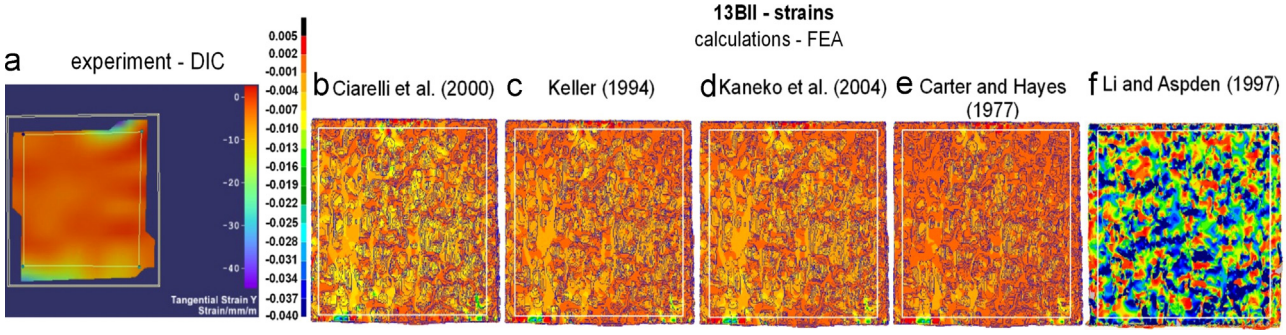


**Fig. 7 – Comparison of strain distributions obtained from (a) experiment (DIC) and (b–f) numerical analyses (FEA) for specimen no. 13BII.**

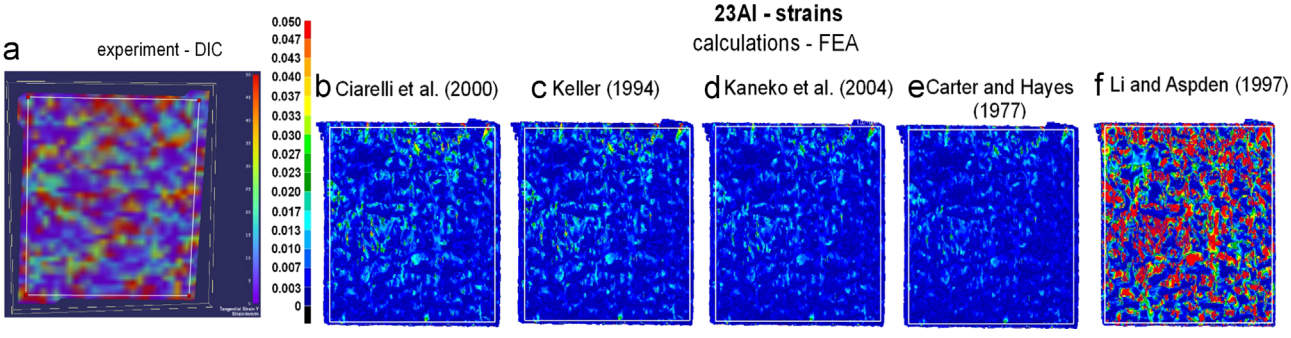


**Fig. 8 – Comparison of strain distributions obtained from (a) experiment (DIC) and (b–f) numerical analyses (FEA) for specimen no. 23AI. The distribution obtained from the relationship given by Li and Aspden (1997) seems to be the most similar to the experimental distribution. In fact, the average strain relative error $\delta_\varepsilon$ is 78.75% (Table 7).**

the movement of the top plate. In this case, the load was applied in five steps of calculation with a linear increase in load.

The results of the numerical analyses were compared with the experimental full-field measurements obtained from the DIC system. Three quantities were compared: the maximum displacement, the displacement in control point A, and the average strain value in the selected area. The control points were placed in the top part of specimens, near the top loading surfaces, where the high displacement values minimized the influence of the reading error on the results (Figs. 5 and 6). The areas in which the average strains were calculated are marked with a white frame on Figs. 7 and 8.

The numerical models were calculated using the MSC. Marc&Mentat 2012 software (MSC Software Corporation, Santa Ana, California, USA) and a symmetric multi-frontal sparse solver. The calculations were run on a PC (Dell T7500 Intel® Xeon® X5650, 2 processors 2.67 GHz, 96 GB RAM).

## 3. Results

The displacement and strain full-field measurements for each specimen were obtained from the numerical analyses and the experiment. The measured values of the maximum displacement, the displacement in control point A and the average strain values in the selected area are presented in Table 7. The displacement and strain distributions for two exemplary specimens are shown in Figs. 5–8. The experimental full-field measurements from the DIC system are shown in Figs. 5a–8a, whereas the other figures show the results of numerical simulations. In the case of perfect accuracy of the numerical simulation, numerical displacement and strain distributions should be identical with the experimental measurements. Therefore, the best accuracy of numerical analysis should be found in the relationship for which obtained numerical displacements and strains distributions were the most similar to the experimental results.

The comparison of the experimental data with the numerical analyses as for the displacement and strain distributions indicates that the best accuracy of the numerical analysis was obtained for the relationship given by Ciarelli et al. (2000) ($\overline{\delta}_{max} = 14.11\%$, $\overline{\delta}_A = 17.87\%$, $\overline{\delta}_\varepsilon = 50.94\%$) as compared to others Keller (1994) ($\overline{\delta}_{max} = 23.20\%$, $\overline{\delta}_A = 25.88\%$, $\overline{\delta}_\varepsilon = 60.27\%$), Kaneko et al. (2004) ($\overline{\delta}_{max} = 29.42\%$, $\overline{\delta}_A = 37.26\%$, $\overline{\delta}_\varepsilon = 62.29\%$), Carter and Hayes (1977) ($\overline{\delta}_{max} = 35.47\%$, $\overline{\delta}_A = 45.18\%$, $\overline{\delta}_\varepsilon = 67.99\%$), Li and Aspden (1997) ($\overline{\delta}_{max} = 328.81\%$, $\overline{\delta}_A = 364.74\%$, $\overline{\delta}_\varepsilon = 216.62\%$). However, the good accuracy for the relationship given by Ciarelli et al. (2000), which allows for practical application, was obtained only for displacement values ($\overline{\delta}_{max} = 14.11\%$, $\overline{\delta}_A = 17.87\%$). Despite this, the calculations also indicate that the accuracy for average strain values was much lower. However, the smallest average relative error for the strain ($\overline{\delta}_\varepsilon = 50.94\%$) was obtained also for the relationship from Ciarelli et al. (2000). Accuracy for the other relationships was even lower.

As the relationship given by Ciarelli et al. (2000) provides the highest accuracy of the numerical analysis of all the relationships taken into account in this study, the relative errors obtained using this relationship were compared for the specimens divided into four categories: “core”, “side”, “tet10”, and “hex8”. The average relative errors calculated for the two categories depending on the position of the specimen in the femoral head were as follows: “core” ($\overline{\delta}_{max}^{core} = 16.25\%$, $\overline{\delta}_A^{core} = 15.75\%$, $\overline{\delta}_\varepsilon^{core} = 47.89\%$), and “side” ($\overline{\delta}_{max}^{side} = 11.11\%$, $\overline{\delta}_A^{side} = 20.83\%$, $\overline{\delta}_\varepsilon^{side} = 55.22\%$). The average relative errors calculated for the categories depending on the type of the finite element used in the numerical model were as follows: “tet10” ($\overline{\delta}_{max}^{tet} = 15.14\%$, $\overline{\delta}_A^{tet} = 19.69\%$, $\overline{\delta}_\varepsilon^{tet} = 57.16\%$) and “hex8” ($\overline{\delta}_{max}^{hex} = 12.67\%$, $\overline{\delta}_A^{hex} = 15.32\%$, $\overline{\delta}_\varepsilon^{hex} = 42.24\%$). These average relative errors show that the accuracy of numerical results for displacements was similar for all the categories (maximum difference of average relative errors for displacements was 5.14% between $\overline{\delta}_{max}^{core}$ and $\overline{\delta}_{max}^{side}$). The maximum difference for strain was higher (14.92% between $\overline{\delta}_\varepsilon^{tet}$ and $\overline{\delta}_\varepsilon^{hex}$), but the values of average relative errors for strains were also much higher. The obtained results indicate that there is no basis to conclude that the accuracy of the numerical solution in this study depended on the specimen's position in the femoral head or on the type of the finite element used in the numerical model.

## 4. Discussion and conclusions

This paper describes the research on the applicability of relationships derived from the macro-scale compression tests for the calculation of Young's modulus distribution of trabeculae in micro-scale. The compression tests of 11 specimens with DIC full-field measurements of displacement and strains were combined with the numerical analyses.

The results of the numerical calculations indicate that most of Young's modulus relationships obtained in macro-scale testing cannot be used in micro-scale. Only the relationship given by Ciarelli et al. (2000) provides a high accuracy of the numerical solution. This is a surprising result, especially that experimenting with new applications of macro-scale's relationships could seem unreasonable. In order to account for these results, the experimental Young's modulus ranges of trabeculae (Choi et al., 1990; Hong et al., 2007; Jiroušek et al., 2011; Rho et al., 1997; Turner et al., 1999; Zysset et al., 1999) need to be compared with Young's modulus distributions calculated in this study using GD values ($GD_{ij}^{(sn)}$) obtained from micro-CT scans and calibration curves for each specimen (Table 6). Young's modulus distributions for each specimen calculated from the relationship given by Li and Aspden (1997) were too narrow and limited to the range of 0.277–1.695 GPa. This range was significantly below the lower limits of the experimental ranges of Young's modulus of trabeculae (Choi et al., 1990; Hong et al., 2007; Jiroušek et al., 2011; Rho et al., 1997; Turner et al., 1999; Zysset et al., 1999). Therefore, applying this relationship to the numerical calculations causes too low stiffness of the numerical model, resulting in large displacements and deformations. Also, the results of numerical calculations are highly different from the experimental data for this relationship (Table 7). On the other hand, Young's modulus distributions for each specimen calculated from the relationship given by Carter and Hayes (1977) were included in the range of 0.532–75.753 GPa, which is too wide compared to the experimental ranges (Choi et al., 1990; Hong et al., 2007; Jiroušek et al., 2011; Rho et al., 1997;

**Table 7 – Comparison of experimental (DIC) and numerical (FEA) results.**

The comparison of experimental (DIC) and numerical (FEA) results

| | | Absolute value of maximum displacements [mm] | | | Absolute value of displacements in control point A [mm] | | | Absolute value of average strain y-component | | |
|---|---|---|---|---|---|---|---|---|---|---|
| Specimen number | Relationship | Experiment (DIC) | FEA | Relative error $\delta_{max}$ [%] | Experiment (DIC) | FEA | Relative error $\delta_A$ [%] | Experiment (DIC) | FEA | Relative error $\delta_\varepsilon$ [%] |
| 8AII | Ciarelli et al. (2000) | 0.17 | 0.195 | 14.71 | 0.164 | 0.112 | 31.71 | 0.0108 | 0.0028 | 74.02 |
| | Keller (1994) | | 0.189 | 11.18 | | 0.106 | 35.37 | | 0.0025 | 76.57 |
| | Carter and Hayes (1977) | | 0.169 | 0.59 | | 0.044 | 73.17 | | 0.0016 | 84.92 |
| | Kaneko et al. (2004) | | 0.172 | 1.18 | | 0.049 | 70.12 | | 0.0018 | 83.67 |
| | Li and Aspden (1997) | | 0.636 | 274.12 | | 0.457 | 178.66 | | 0.0131 | 21.61 |
| 12AI | Ciarelli et al. (2000) | 0.08 | 0.077 | 3.75 | 0.08 | 0.055 | 31.25 | 0.003 | 0.0026 | 13.87 |
| | Keller (1994) | | 0.079 | 1.25 | | 0.057 | 28.75 | | 0.0027 | 11.44 |
| | Carter and Hayes (1977) | | 0.065 | 18.75 | | 0.045 | 43.75 | | 0.002 | 34.98 |
| | Kaneko et al. (2004) | | 0.063 | 21.25 | | 0.042 | 47.50 | | 0.0021 | 30.59 |
| | Li and Aspden (1997) | | 0.332 | 315.00 | | 0.287 | 258.75 | | 0.0149 | 397.74 |
| 12BII | Ciarelli et al. (2000) | 0.24 | 0.164 | 31.67 | 0.103 | 0.084 | 18.45 | 0.0064 | 0.0031 | 51.42 |
| | Keller (1994) | | 0.127 | 47.08 | | 0.063 | 38.83 | | 0.0027 | 58.23 |
| | Carter and Hayes (1977) | | 0.113 | 52.92 | | 0.052 | 49.51 | | 0.002 | 68.60 |
| | Kaneko et al. (2004) | | 0.114 | 52.50 | | 0.056 | 45.63 | | 0.0021 | 67.00 |
| | Li and Aspden (1997) | | 0.384 | 60.00 | | 0.314 | 204.85 | | 0.0183 | 185.22 |
| 13BII | Ciarelli et al. (2000) | 0.09 | 0.077 | 14.44 | 0.06 | 0.054 | 10.00 | 0.003 | 0.0025 | 18.01 |
| | Keller (1994) | | 0.048 | 46.67 | | 0.034 | 43.33 | | 0.0013 | 56.31 |
| | Carter and Hayes (1977) | | 0.031 | 65.56 | | 0.018 | 70.00 | | 0.0007 | 77.19 |
| | Kaneko et al. (2004) | | 0.05 | 44.44 | | 0.034 | 43.33 | | 0.0014 | 52.54 |
| | Li and Aspden (1997) | | 0.44 | 388.89 | | 0.375 | 525.00 | | 0.0112 | 272.40 |
| 14AII | Ciarelli et al. (2000) | 0.1 | 0.104 | 4.00 | 0.067 | 0.083 | 23.88 | 0.0045 | 0.0037 | 17.51 |
| | Keller (1994) | | 0.068 | 32.00 | | 0.054 | 19.40 | | 0.0026 | 43.20 |
| | Carter and Hayes (1977) | | 0.044 | 56.00 | | 0.035 | 47.76 | | 0.0014 | 68.19 |
| | Kaneko et al. (2004) | | 0.062 | 38.00 | | 0.05 | 25.37 | | 0.0021 | 52.36 |
| | Li and Aspden (1997) | | 0.512 | 412.00 | | 0.423 | 531.34 | | 0.0157 | 248.22 |
| 15AII | Ciarelli et al. (2000) | 0.105 | 0.071 | 32.38 | 0.1 | 0.07 | 30.00 | 0.02 | 0.0026 | 86.94 |
| | Keller (1994) | | 0.064 | 39.05 | | 0.06 | 40.00 | | 0.0022 | 89.17 |

Table 7 (*continued*)

| The comparison of experimental (DIC) and numerical (FEA) results | | | | | | | | | | |
|---|---|---|---|---|---|---|---|---|---|---|
| | | Absolute value of maximum displacements [mm] | | | Absolute value of displacements in control point A [mm] | | | Absolute value of average strain y-component | | |
| Specimen number | Relationship | Experiment (DIC) | FEA | Relative error $\delta_{max}$ [%] | Experiment (DIC) | FEA | Relative error $\delta_A$ [%] | Experiment (DIC) | FEA | Relative error $\delta_\varepsilon$ [%] |
| | Carter and Hayes (1977) | | 0.05 | 52.38 | | 0.046 | 54.00 | | 0.0016 | 91.93 |
| | Kaneko et al. (2004) | | 0.054 | 48.57 | | 0.053 | 47.00 | | 0.002 | 89.79 |
| | Li and Aspden (1997) | | 0.412 | 292.38 | | 0.375 | 275.00 | | 0.0172 | 13.80 |
| 16BII | Ciarelli et al. (2000) | 0.2 | 0.169 | 15.50 | 0.19 | 0.154 | 18.95 | 0.013 | 0.0059 | 54.53 |
| | Keller (1994) | | 0.149 | 25.50 | | 0.135 | 28.95 | | 0.0031 | 76.39 |
| | Carter and Hayes (1977) | | 0.101 | 49.50 | | 0.091 | 52.11 | | 0.0034 | 73.99 |
| | Kaneko et al. (2004) | | 0.122 | 39.00 | | 0.11 | 42.11 | | 0.0042 | 67.81 |
| | Li and Aspden (1997) | | 0.606 | 203.00 | | 0.552 | 190.53 | | 0.0133 | 2.47 |
| 17AII | Ciarelli et al. (2000) | 0.125 | 0.153 | 22.40 | 0.115 | 0.136 | 18.26 | 0.006 | 0.0028 | 52.86 |
| | Keller (1994) | | 0.147 | 17.60 | | 0.13 | 13.04 | | 0.0027 | 54.91 |
| | Carter and Hayes (1977) | | 0.114 | 8.80 | | 0.098 | 14.78 | | 0.002 | 66.21 |
| | Kaneko et al. (2004) | | 0.117 | 6.40 | | 0.102 | 11.30 | | 0.0021 | 64.82 |
| | Li and Aspden (1997) | | 0.869 | 595.20 | | 0.807 | 601.74 | | 0.0195 | 225.38 |
| 18CI | Ciarelli et al. (2000) | 0.14 | 0.13 | 7.14 | 0.09 | 0.09 | 0.00 | 0.004 | 0.0057 | 43.16 |
| | Keller (1994) | | 0.129 | 7.86 | | 0.088 | 2.22 | | 0.0056 | 39.46 |
| | Carter and Hayes (1977) | | 0.105 | 25.00 | | 0.065 | 27.78 | | 0.0042 | 5.97 |
| | Kaneko et al. (2004) | | 0.106 | 24.29 | | 0.067 | 25.56 | | 0.0043 | 8.04 |
| | Li and Aspden (1997) | | 0.711 | 407.86 | | 0.626 | 595.56 | | 0.0368 | 819.08 |
| 20BII | Ciarelli et al. (2000) | 0.22 | 0.201 | 8.64 | 0.2 | 0.182 | 9.00 | 0.0068 | 0.0025 | 63.63 |
| | Keller (1994) | | 0.18 | 18.18 | | 0.161 | 19.50 | | 0.0018 | 74.13 |
| | Carter and Hayes (1977) | | 0.16 | 27.27 | | 0.141 | 29.50 | | 0.0011 | 84.53 |
| | Kaneko et al. (2004) | | 0.173 | 21.36 | | 0.153 | 23.50 | | 0.0015 | 77.75 |

| | | | | | | | | | | | |
|---|---|---|---|---|---|---|---|---|---|---|---|
| | Li and Aspden (1997) | | 0.953 | 333.18 | | 0.934 | 367.00 | | 0.0221 | 224.88 |
| 23AI | Ciarelli et al. (2000) | 0.2 | 0.186 | 7.00 | 0.182 | 0.172 | 5.49 | 0.0126 | 0.004 | 68.30 |
| | Keller (1994) | | 0.162 | 19.00 | | 0.149 | 18.13 | | 0.0034 | 73.13 |
| | Carter and Hayes (1977) | | 0.116 | 42.00 | | 0.106 | 41.76 | | 0.0024 | 81.19 |
| | Kaneko et al. (2004) | | 0.134 | 33.00 | | 0.123 | 32.42 | | 0.0028 | 77.51 |
| | Li and Aspden (1997) | | 0.905 | 352.50 | | 0.858 | 371.43 | | 0.0225 | 78.75 |
| 24AII | Ciarelli et al. (2000) | 0.13 | 0.12 | 7.69 | 0.126 | 0.104 | 17.46 | 0.0109 | 0.0036 | 67.06 |
| | Keller (1994) | | 0.113 | 13.08 | | 0.097 | 23.02 | | 0.0032 | 70.29 |
| | Carter and Hayes (1977) | | 0.095 | 26.92 | | 0.078 | 38.10 | | 0.0024 | 78.16 |
| | Kaneko et al. (2004) | | 0.1 | 23.08 | | 0.084 | 33.33 | | 0.0027 | 75.63 |
| | Li and Aspden (1997) | | 0.535 | 311.54 | | 0.475 | 276.98 | | 0.0229 | 109.92 |

Turner et al., 1999; Zysset et al., 1999). As a result, the stiffness of the numerical models was high, which resulted in significantly lower displacements and deformations than in the experiment. Therefore, applying both Li and Aspden (1997) and/or Carter and Hayes (1977) relationships provides extreme Young's modulus distributions, which are too narrow or too wide, respectively. The relationships given by Ciarelli et al. (2000), Keller (1994) and Kaneko et al. (2004) provide Young's modulus distributions more similar to the experimental ranges (Choi et al., 1990; Hong et al., 2007; Jiroušek et al., 2011; Rho et al., 1997; Turner et al., 1999; Zysset et al., 1999), which are 1.461–11.829 GPa, 0.548–32.444 GPa and 1.365–24.048 GPa, respectively. The highest accuracy of numerical calculations is obtained using the Ciarelli et al. (2000) relationship with Young's modulus distributions within the range of 1.461–11.829 GPa, which is the most similar to the experimental ranges given by Choi et al. (1990), Hong et al. (2007) and Zysset et al. (1999). This accounts for the high accuracy of the numerical calculations obtained using this relationship, especially that the compression tests and measurement of these experimental ranges in the studies (Choi et al., 1990; Hong et al., 2007; Zysset et al., 1999) were both performed in wet conditions.

Apart from Young's modulus, Poisson's ratio also had an influence on the solution of the numerical calculation. In this study Poisson's ratio of 0.3 was used, but it was an assumption taken based on other numerical studies of the human femur in the literature (Couteau et al., 1998; Nareliya and Kumar, 2011; Sherekar and Pawar, 2013; Trabelsi et al., 2011). In contradiction to this, the experimentally determined value of Poisson's ratio of microscopic cubic specimens in three different directions was reported by Hong et al. (2007). They reported Poisson's ratio of 0.199 (longitudinal), 0.152 (anterior–posterior) and 0.154 (latero-medial). This shows a big difference between the commonly used value of 0.3 of Poisson's ratio and the values determined experimentally. Therefore, accuracy of the numerical calculations can be increased using the experimentally determined values of Poisson's ratio rather than Poisson's ratio of 0.3 commonly used in the literature.

There are also many other factors that could influence our experiments such as fixing in ethanol, a testing in the air, painting of the specimens and the radiation dose. The negative influence of fixation in ethanol on the specimens was presented by Hammer et al. (2014), where alterations of the mechanical properties of bone specimens were observed during long-term immersion in ethanol. However, we tried to minimize the time of specimen's fixation in ethanol, which was several hours. The other factor was a testing in the air. During the compression tests, the air partially filled the pores between the trabeculae instead of the bone marrow. The bone marrow remaining in the interaction with trabeculae affects the mechanical properties of trabeculae and also carries the external loads. However, our research was focused on a micro-scale and the mechanical properties of trabeculae without taking into account a bone marrow contained in the pores between trabeculae (this is rather a meso-scale). Thus, the ability of carrying external loads by a bone marrow contained in the pores is less important in our research. However, the interaction of bone marrow and trabeculae and

the possible changes of mechanical properties of trabeculae caused by an air presence instead of bone marrow could significantly influence the obtained results. Painting of the specimens could also make some disturbances on the measured values of displacements and strains as the used acrylic paint could also carry the applied loads. Only one side surface of each specimen was painted, so there was no obstacle for marrow escape during compression tests. However, the average depth of the penetration of acrylic paint into the specimens equaled to less than 1 mm (Fig. 2c). In this region the pores were filled with acrylic paint and this could affect the mechanical behavior of the specimens. Young's modulus of acrylic paint is significantly lower than Young's modulus of trabeculae and is approximately equal to $E=1$ GPa (Wright et al., 2014). A 1 mm-thin layer of acrylic paint that Young's modulus is significantly lower than Young's modulus of trabeculae might make its impact negligible. Effect of radiation dose on the mechanical behavior of specimens could also make it negligible. This is proved by the work of Currey et al. (1997), in which the effects of ionizing radiation on, inter alia, mechanical properties of human bone were examined. Young's modulus was unchanged by any level of radiation. Similarly, in the work of Barth et al. (2011), on the basis of the obtained stress–strain curves from the three-point bending test, it can be concluded that Young's moduli are constant for various degrees of X-ray irradiation. In addition, Brouwers et al. (2007) found no effects of micro-CT radiation on structural parameters of bone, which we also analyzed in our research.

The application of the relationship by Ciarelli et al. (2000) to the numerical calculation allows one to obtain the displacement distribution with a relative error of 17.87%. In the strain distribution the relative error is much higher and is about 50.94%. Therefore, the relationship given by Ciarelli et al. (2000) is not dedicated to determine the strain and stress in the bone. Although this study involved the numerical analyses only in the elastic range, it could be concluded that the application of this relationship in nonlinear simulations such as cracking, where the accuracy of determined stress concentrations should be very high, is not to be recommended, either. However, the application of the Ciarelli et al. (2000) relationship in the linear simulations is possible, but only to determine displacement.

The comparison of average relative errors for categories: “core”, “side”, “tet10” and “hex8” indicates that there is no basis to conclude that the accuracy of the numerical solution in this study depended on the specimen's position in the femoral head or the type of the finite element used in the numerical model. What could influence the results of the calculations were the mesh density and the boundary conditions. The results of the numerical calculations were obtained using the number of elements from the range of 750,000–1,250,000 (Table 5). Therefore, increasing the number of elements or using the adaptive finite element techniques can provide a higher accuracy of calculations, but the computing time will be extended. The appropriate selection of boundary conditions has the greatest impact on the accuracy of calculations. In this study the boundary conditions represented a mechanical compression test in which a platen technique was used. As a result, the compression of the specimens could be influenced by the end artifacts and friction between ends of specimens and platens. However, a DIC system was used that measures the displacement and strain distributions on the specimen's surface and even they are influenced by the end artifact and friction. As a result on the obtained maps of displacement and strain distributions concentrations of displacements/strains caused by these end artifacts are visible (e.g. the concentration of the displacements and strains visible in the top part of Figs. 5a and 7a). Thus, the end artifacts influence our results, but this influence is measured by the DIC system, thereby causing the accuracy of the measurements to be limited to the accuracy of the DIC system. However, the representation of these boundary conditions (end artifacts, friction) in the numerical simulation can be a bigger problem. Although the representation of the end artifacts in the FE models of specimens was quite accurate as we have the voxel size of 10.246 μm in the micro-CT scans, the inaccuracy could appear in modeling of friction. We used in the FE models the glue contact between the plates and mesh of the bone structure. This simplification could influence the obtained numerical results, especially for strains, and as a result the calculated average relative errors for strains. The use of touching contact with an accurately determined value of friction coefficient may slightly increase the estimated accuracy of numerical simulations.

## Acknowledgments

The authors would like to thank Jolanta Filipek for her help using the Mimics 15.0 and Anna Wójcicka for help in the analysis of speckle patterns. The numerical simulations were calculated using the license for MSC.Software provided by the Academic Computer Centre in Gdańsk, Poland. Łukasz Cyganik and Paulina Popik are beneficiaries of the “Silesian Cooperation: Innovations For Efficient Development (SWIDER)” project realized within Human Capital Operational Programme, Priority VIII: Regional human resources for the economy, 8.2 Transfer of knowledge, Sub-measure 8.2.1 Support for cooperation of scientific environment and enterprises. The project was partially funded from European Union Project based on European Social Funds 8.2.1. Marcin Binkowski was partially supported by postdoctoral fellowship (KOLUMB) and supportive Grant from the Foundation for Polish Science, Warsaw, Poland.

The project was partially supported by Grant no. N N518 425036 from the Ministry of Science and Higher Education, Warsaw, Poland.

## REFERENCES

Augat, Peter, Link, Thomas, Lang, Thomas F., Lin, John C., Majumdar, Sharmila, Genant, Harry K., 1998. Anisotropy of the elastic modulus of trabecular bone specimens from different anatomical locations. Med. Eng. Phys. 20, 124–131.

Badde, A., Illerhaus, B., 2008. Three dimensional computerized microtomography in the analysis of sculpture. Scanning 30, 16–26.

Barth, Holly D., Zimmermann, Elizabeth A., Schaible, Eric, Tang, Simon Y., Alliston, Tamara, Ritchie, Robert O., 2011.

Characterization of the effects of X-ray irradiation on the hierarchical structure and mechanical properties of human cortical bone. Biomaterials 32, 34.
Becker, T., Splitthof, K., Siebert, T., Kletting, P., 2006. Technical Note – T-Q-400-Accuracy-3DCORR-003-EN. Dantec Dynamics GmbH, Germany.
Binkowski, M., G.R., Davis, Z., Wrobel, A.E., Goodship, 2010. Quantitative measurement of the bone density by X-ray microcomputed tomography. In: Proceedings of the 6th World Congress of Biomechanics, vol. 31, pp. 856–859.
Binkowski, M., G., Kokot, F., Bolechala, A., John, 2012. Image-based finite element modeling of the three-point bending test of cortical bone. In: Proceedings of SPIE 8506, Developments in X-Ray Tomography VIII, 85060D.
Brouwers, Julienne E.M., Rietbergen, Bert Van, Huiskes, Rik, 2007. No effects of in vivo micro-CT radiation on structural parameters and bone marrow cells in proximal tibia of wistar rats detected after eight weekly scans. J. Orthop. Res. 25, 1325–1332, http://dx.doi.org/10.1002/jor.
Carter, D.R., Hayes, W.C., 1977. The compressive behavior of bone as a two-phase porous structure. J. Bone Jt. Surg. 59 (7), 954–962.
Choi, K., Kuhn, J.L., Ciarelli, M.J., Goldstein, S.A., 1990. The elastic moduli of human subchondral, trabecular, and cortical bone tissue and the size-dependency of cortical bone modulus. J. Biomech. 23 (11), 1103–1113.
Ciarelli, T.E., Fyhrie, D.P., Schaffler, M.B., Goldstein, S.A., 2000. Variations in three-dimensional cancellous bone architecture of the proximal femur in female hip fractures and in controls. J. Bone Miner. Res. 15 (1), 32–40.
Couteau, B., Hobatho, M.C., Darmana, R., Brignola, J.C., Arlaud, J.Y., 1998. Finite element modelling of the vibrational behaviour of the human femur using CT-based individualized geometrical and material properties. J. Biomech. 31 (4), 383–386.
Currey, J.D., Foreman, J., Laketić, I., Mitchell, J., Pegg, D.E., Reilly, G. C., 1997. Effects of ionizing radiation on the mechanical properties of human bone. J. Orthop. Res.: Off. Publ. Orthop. Res. Soc. 15 (1), 111–117.
Depalle, B., Chapurlat, R., Walter-Le-Berre, H., Bou-Saïd, B., Follet, H., 2013. Finite element dependence of stress evaluation for human trabecular bone. J. Mech. Behav. Biomed. Mater. 18, 200–212.
van Garderen, N., Clemens, F.J., Kaufmann, J., Urbanek, M., Binkowski, M., Graule, T., Aneziris, C.G., 2012. Pore analyses of highly porous diatomite and clay based materials for fluidized bed reactors. Microporous Mesoporous Mater. 151, 255–263.
Hambli, Ridha, 2013. Micro-CT finite element model and experimental validation of trabecular bone damage and fracture. Bone 56 (2), 363–374.
Hammer, Niels, Voigt, Christian, Werner, Michael, Hoffmann, Falk, Bente, Klaus, Kunze, Holger, Scholz, Roger, Steinke, Hanno, 2014. Ethanol and formaldehyde fixation irreversibly alter bones' organic matrix. J. Mech. Behav. Biomed. Mater. 29, 252–258.
Helgason, B., Perilli, E., Schileo, E., Taddei, F., Brynjólfsson, S., Viceconti, M., 2008. Mathematical relationships between bone density and mechanical properties: a literature review. Clin. Biomech. (Bristol, Avon) 23 (2), 135–146.
Hong, J., Cha,H., Park, Y., Lee, S., Khang, G., Kim, Y., 2007. Elastic moduli and Poisson's ratios of microscopic human femoral trabeculae. In: Proceedings of 11th Mediterranean Conference on Medical and Biomedical Engineering and Computing 2007, IFMBE, vol. 16, pp. 274–277.
Jiroušek, O., Němeček, J., Kytýř, D., Kunecký, J., Zlámal, P., Doktor, T., 2011. Nanoindentation of trabecular bone – comparison with uniaxial testing of single trabecula. Chem. Listy 105, 668–671.
Kaneko, T.S., Bell, J.S., Pejcic, M.R., Tehranzadeh, J., Keyak, J.H., 2004. Mechanical properties, density and quantitative CT scan data of trabecular bone with and without metastases. J. Biomech. 37 (4), 523–530.
Kanis, J.A., Johnell, O., Oden, A., Jonsson, B., De Laet, C., Dawson, A., 2000. Risk of hip fracture according to the World Health Organization criteria for osteopenia and osteoporosis. Bone 27 (5), 585–590.
Keller, T.S., 1994. Predicting the compressive mechanical behavior of bone. J. Biomech. 27 (9), 1159–1168.
Keyak, J.H., Lee, I.Y., Skinner, H.B., 1994. Correlations between orthogonal mechanical properties and density of trabecular bone: use of different densitometric measures. J. Biomed. Mater. Res. 28, 1329–1336.
Kokot, G., Binkowski, M., John, A., Gzik-Zroska, B., 2012. Advanced mechanical testing methods in determining bone material properties. Mechanika: Proceedings of the 17th International Conference, Kaunas, 139–143.
Li, B., Aspden, R.M., 1997. Composition and mechanical properties of cancellous bone from the femoral head of patients with osteoporosis or osteoarthritis. J. Bone Miner. Res. 12 (4), 641–651.
Lin, A.S., Barrows, T.H., Cartmell, S.H., Guldberg, R.E., 2003. Microarchitectural and mechanical characterization of oriented porous polymer scaffolds. Biomaterials 24 (0142–9612), 481–489.
Łukowski, J., Kaczmarek, M., Kubik, J., 2000. Anisotropic properties of trabecular bone. Conductometric and ultrasonic studies. Acta Bioeng. Biomech. 2 (1), 17–27.
Makowski, P., John, A., Kuś, W., Kokot, G., 2013. Multiscale modeling of the simplified trabecular bone structure. Mechanika: Proceedings of the 18th International Conference, Kaunas, 156–161.
McDonald, S.A., Preuss, M., Maire, E., Buffiere, J.Y., Mummery, P. M., Withers, P.J., 2003. X-ray tomographic imaging of Ti/SiC composites. J. Microsc. 209 (0022–2720), 102–112.
Mercer, C.E., Anderson, P., Davis, G.R., 2003. Sequential 3D X-ray microtomographic measurement of enamel and dentine ablation by an Er:YAG laser. Br. Dent. J. 194 (2), 99–104.
Muller, R., Van Campenhout, H., Van Damme, B., Van Der Perre, G., Dequeker, J., Hildebrand, T., Ruegsegger, P., 1998. Morphometric analysis of human bone biopsies: a quantitative structural comparison of histological sections and micro-computed tomography. Bone 23 (1), 59–66.
Nareliya, R., Kumar, V., 2011. Biomechanical analysis of human femur bone. Int. J. Eng. Sci. Technol. 3 (4), 3090–3094.
Rho, J.Y., Tsui, T.Y., Pharr, G.M., 1997. Elastic properties of human cortical and trabecular lamellar bone measured by nanoindentation. Biomaterials 18 (20), 1325–1330.
Rüegsegger, P., Koller, B., Müller, R., 1996. A microtomographic system for the nondestructive evaluation of bone architecture. Calcif. Tissue Int. 58 (1), 24–29.
Shefelbine, S.J., Simon, U., Claes, L., Gold, A., Gabet, Y., Bab, I., Muller, R., Augat, P., 2005. Prediction of fracture callus mechanical properties using micro-CT images and voxel-based finite element analysis. Bone 36 (3), 480–488.
Sherekar, R.M., Pawar, A.N., 2013. Numerical analysis of human femoral bone in different phases. Int. J. Eng. Innov. Technol. 2 (12), 76–80.
Trabelsi, N., Yosibash, Z., Wutte, Ch., Augat, P., Eberle, S., 2011. Patient-specific finite element analysis of the human femur – a double-blinded biomechanical validation. J. Biomech. 44 (9), 1666–1672.

Turner, C.H., Rho, J., Takano, Y., Tsui, T.Y., Pharr, G.M., 1999. The elastic properties of trabecular and cortical bone tissues are similar: results from two microscopic measurement techniques. J. Biomech. 32 (4), 437–441.

Ulrich, D., van Rietbergen, B., Weinans, H., Ruegsegger, P., 1998. Finite element analysis of trabecular bone structure: a comparison of image-based meshing techniques. J. Biomech. 31 (12), 1187–1192.

WHO, 1994. Assesment of fracture risk and its applications to screening for postemnopausal osteoporosis. World Health Organization. ⟨http://www.who.int/bookorders/anglais/detart1.jsp?sesslan=1&codlan=1&codcol=10&codcch=843⟩.

Wagner, David W., Lindsey, Derek P., Beaupre, Gary S., 2011. Deriving tissue density and elastic modulus from microCT bone scans. Bone 49 (5), 931–938.

Wright, Madeleine S., Hudson, Maggie, Kokkori, Maria, Muir, Kim, Casadio, Francesca, Faber, Katherine T., Shull, Kenneth R., 2014. Quantifying the mechanical properties of artists' paints with nanoindentation. In: Proceedings of the 2014 Annual Meeting of the Adhesion Society.

Zysset, P.K., Guo, X.E., Hoffler, C.E., Moore, K.E., Goldstein, S.A., 1999. Elastic modulus and hardness of cortical and trabecular bone lamellae measured by nanoindentation in the human femur. J. Biomech. 32 (10), 1005–1012.